Chinese Journal of Aeronautics 24 (2011) 648-656

Contents lists available at ScienceDirect

Chinese Journal of Aeronautics

journal homepage: www.elsevier.com/locate/cja

Improved Angular Velocity Estimation Using MEMS Sensors with Applications in Miniature Inertially Stabilized Platforms

ZHOU Xiaoyao, ZHANG Zhiyong*, FAN Dapeng

College of Mechatronics and Automation, National University of Defense Technology, Changsha 410073, China

Received 9 May 2011; revised 23 June 2011; accepted 8 July 2011

Abstract

The performance of any inertially stabilized platform (ISP) is strongly related to the bandwidth and accuracy of the angular velocity signals. This paper discusses the development of an optimal state estimator for sensing inertial velocity using low-cost micro-electro-mechanical systems (MEMS) sensors. A low-bandwidth gyroscope is used alone with two low-performance accelerometers to obtain the estimation. The gyroscope has its own limited dynamics and mainly contributes to the low-frequency components of the estimation. The accelerometers have inherent biases and mainly contribute to the high-frequency components of the estimation. Extensive experimental results show that the state estimator can achieve high-performance signals over a wide range of velocities without drifts in both the *t*- and *s*-domains. Furthermore, with applications in miniature inertially stabilized platforms, the control characteristic presents a significantly improvement over the existing methods. The method can be also applied to robotics, attitude estimation, and friction compensation.

Keywords: angular velocity; low-cost sensor; gyroscope; accelerometer; Kalman filter; inertially stabilized platform

1. Introduction

Inertially stabilized platforms (ISPs) are routinely used on vehicles, ships, aircraft and spacecraft for diverse missions including aerial photography [1], battle reconnaissance [2], antenna stabilization [3] and missile guidance [4]. This platform requires accurate angular velocity estimation at a relatively high bandwidth to achieve stable control of the lines of sight of optical imaging sensors. This paper discusses the development of an optimal state estimator meant to produce accurate angular velocity signals using low-cost micro-electro-mechanical systems (MEMS) sensors. We focus our attention on planar motions because sensing in three dimensions first requires sensing on the plane [5].

There are many methods of obtaining angular velocity in an inertial reference frame. One common technique is the use of a gyroscope alone, but high-performance sensors, such as laser gyroscopes, fiber optic gyroscopes and dynamically tuned gyroscopes, are too expensive and overburdened with applications for low-cost mini-ISP. The emerging MEMS sensor provides an attractive option because of its size, weight and cost advantages [6], but the low-cost MEMS gyroscope has its own dynamics, limited bandwidth and predominantly high-frequency noise. It cannot provide accurate information over a wide range of velocities. A less common approach is to employ accelerometers to infer the angular acceleration, and this approach is also called gyro-free or non-gyro methods in those papers for attitude detection [7-10]. In theory, integrating angular acceleration calculated by the outputs of accelerometers provides accurate velocity information, even when the platform is moving quickly. In practice, low-cost MEMS accelerometers have an unknown bias or scaling in their outputs, as well as signal noise, causing the integrated results of the velocity estimation

*Corresponding author. Tel.: +86-731-84574934.
E-mail address: zzynihao@126.com
Foundation item: National Natural Science Foundation of China (50805144)

doi: 10.1016/S1000-9361(11)60076-9

to suffer from drift term. This means that it is not practical to sense velocity using accelerometers alone. A third method is to combine the measurements from various sensors. Zhu [11] and Jeon [12], et al. designed an algorithm to estimate angular velocity in body reference frame by fusing encoder and accelerometer outputs. The encoder mainly contributes to the low-frequency components, and the accelerometer mainly contributes to the high-frequency components. The same methodology was used by Leavitt, et al. [13] for sensing inclination angle using gyroscopes and accelerometers. In addition, Rehbinder [14] and Ojeda [15], et al. proposed an improved estimator for sensing attitude in three dimensions. However, the methods mentioned above are only suitable for sensing angular velocity in the body frame or angle in the inertial space. No angular velocity estimation approach related to the inertial space has yet been reported. Because of the requirements of our low-cost mini-ISP, we need to develop significantly improved velocity estimation in the inertial space.

Our method is different from previous approaches in four main aspects: 1) it develops a novel hybrid system, which includes a CS-ARS-02 MEMS gyroscope (cost about $260, Chinastar M&S Limited Corporation) and two ADXL001-70 MEMS accelerometers (cost about $30 each, Analog Devices); 2) an optimal estimator proves to be stochastically uniformly asymptotically stable, allows the system to achieve high-performance angular velocity in the inertial space; 3) the inherent bias of acceleration can be identified and compensated online; 4) with applications in the mini-ISP, the control characteristic has been significantly improved.

2. Analysis of Sensor Performance

2.1. Experimental setup

Fig. 1 shows the schematic diagram of experimental setup, which includes a host PC, a dSPACE 1104 real-time operating system, a power amplifier board, and a test apparatus of one degree-of-freedom mini-ISP, as shown in Fig. 2.

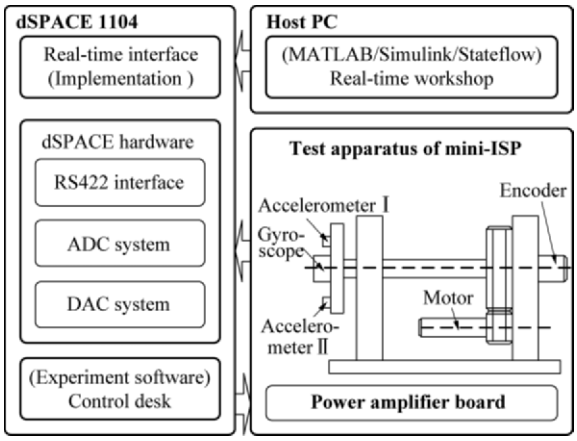

Fig. 1 Schematic diagram of experimental setup.

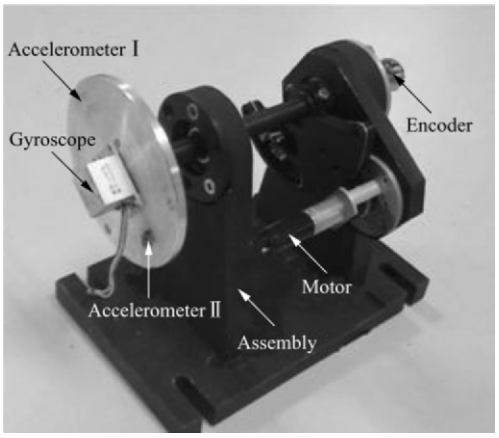

Fig. 2 Test apparatus of one degree-of-freedom mini-ISP.

A micro blush motor 0816-08-3 from Faulhaber is axially assembled with a 29-bit high-resolution encoder specially ordered from AEDA Avago. The control signals for driving the motor are produced by a dSPACE 1104 DAC system and realized by the power amplifier board. A CS-ARS-02 MEMS gyroscope and two ADXL001-70 MEMS accelerometers, whose relative size and typical parameters are shown in Fig. 2 and Table 1, respectively, are mounted on the rotating plane of the test apparatus. These sensors are connected to dSPACE 1104 RS422 and ADC system with real-time interface, thus enabling precise data acquisition. The experiment runs on a dSPACE 1104 real-time operating system based on MATLAB/Simulink at 1 000 Hz sampling rate.

Table 1 Typical parameters of low-cost MEMS sensors

Parameter	Accelerometer (ADXL001-70)	Gyroscope (CS-ARS-02)
Scale factor	24.2 mV/g	15 mV·((°)·s^{-1})$^{-1}$
Bandwidth	32 kHz	60 Hz
Bias/offset	2.5 V	2.5 V
Noise (typical)	2.15g	0.064 (°)/s

2.2. Gyroscope

The outputs of MEMS gyroscope with slow dynamics can be expressed in the s-domain as follows [2]:

$$X_g(s) = G_g(s)(X(s) + W_g(s)) \quad (1)$$

where $X(s)$ is the actual angular velocity, $X_g(s)$ the output of the gyroscope with measured noise $W_g(s)$, and $G_g(s)$ the dynamic model of the gyroscope. It should be considered that a low-performance MEMS gyroscope is always able to achieve good velocity signals via low-pass filter. Therefore the dynamics model of the gyroscope $G_g(s)$ can be treated as a canonical second-order form:

$$G_g(s) = \frac{\omega_n^2}{s^2 + 2\zeta\omega_n s + \omega_n^2} \quad (2)$$

where ω_n and ζ denote the natural frequency and the damping coefficient of the gyroscope, respectively.

Consequently, the inverse Laplace transform of velocity obtained from the gyroscope channel can be written as

$$\ddot{x}_g(t)=\omega_n^2 x(t)-2\zeta\omega_n\dot{x}_g(t)-\omega_n^2 x_g(t)+\omega_n^2 w_g(t) \quad (3)$$

where $x(t)$, $x_g(t)$ and $w_g(t)$ are the inverse Laplace transforms of the $X(s)$, $X_g(s)$ and $W_g(s)$, respectively, in the t-domain.

To investigate the estimation of our gyroscope, a chirp signal [13] of increasing frequency was produced by dSPACE 1104 to drive the sensors. The chirp signal starts at 1 Hz and ends at 60 Hz over a period of 120 s. The output of our gyroscope (scaled to units of (°)/s) compared to the actual velocity (first derivative of the high-resolution encoder) is shown in Fig. 3(a) and Fig. 3(b). At low frequencies, shown in Fig. 3(a), the velocity signals are mainly influenced by the measured noise of the gyroscope. At high frequencies, shown in Fig. 3(b), the gyroscope exhibits distortion in both magnitude and phase.

A sweep signal is used to identify the dynamics of MEMS gyroscope. Figs. 3(c)-3(d) show the identified

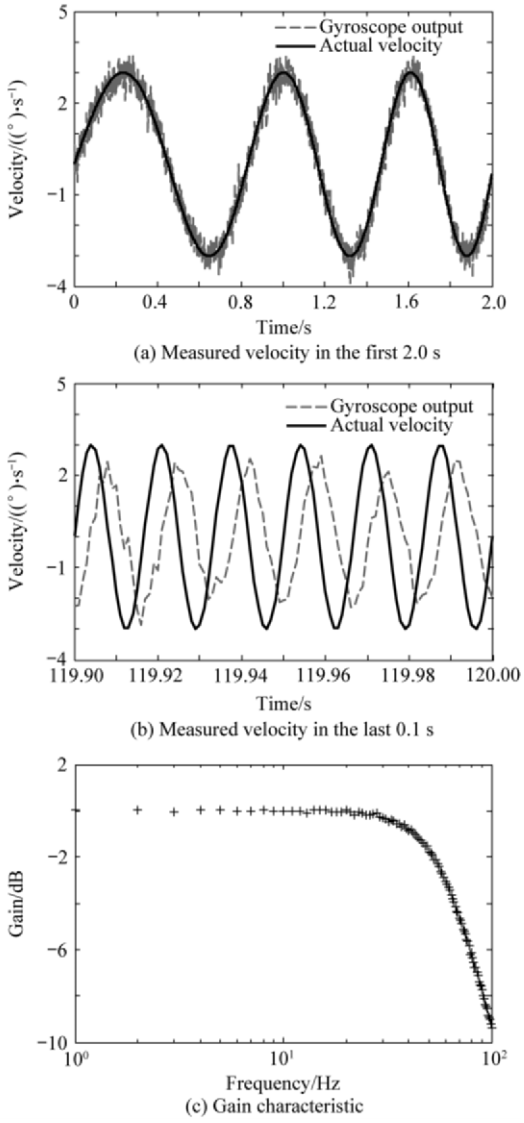

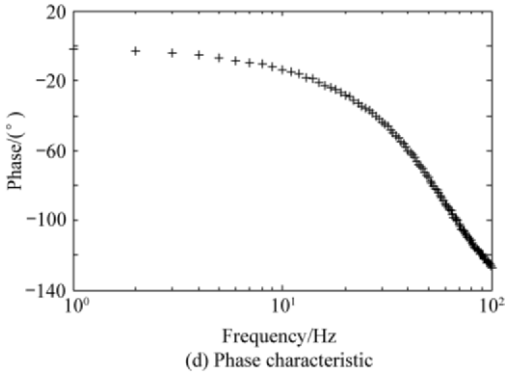

Fig. 3 Measured velocity and transfer function of MEMS gyroscope in chirp motion.

Bode diagram, and a second-order model is adopted to fit the curve within the 1-100 Hz range, with the following transfer function:

$$G_g(s)=\frac{142\,100}{s^2+533.1s+142\,100} \quad (4)$$

2.3. Accelerometer

In order to ascertain angular acceleration, two accelerometers are mounted on the plane 180° apart to eliminate redundant translational acceleration a_t [12], shown in Fig. 4. $\dot{x}(t)$ is the actual angular acceleration, d_1 and d_2 are the distances between the accelerometers and center of rotation.

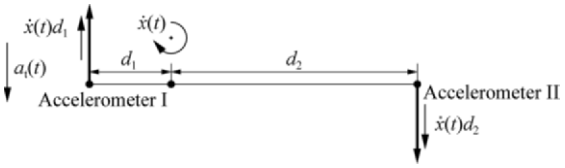

Fig. 4 Accelerometer configuration.

Because the bandwidth of the accelerometer is much higher than that of the gyroscope, the output of accelerometers can be expressed in the t-domain as

$$\begin{cases} a_1(t)=\dot{x}(t)d_1-a_t(t)+b_1(t)+w_1(t) \\ a_2(t)=\dot{x}(t)d_2+a_t(t)+b_2(t)+w_2(t) \end{cases} \quad (5)$$

where $a_1(t)$ and $a_2(t)$ are the measured linear acceleration of each accelerometer; $b_1(t)$, $b_2(t)$, $w_1(t)$ and $w_2(t)$ are the bias and noise components of each accelerometer. In order to compensate for redundant translational acceleration $a_t(t)$, which arises from movement, we can simply calculate the sum of the two equations in Eq. (5) as follows:

$$\dot{x}_a(t)=\dot{x}(t)+b(t)+w_a(t) \quad (6)$$

where $\dot{x}_a(t)=(a_1(t)+a_2(t))/d$ denotes the output of accelerometers, $b(t)=(b_1(t)+b_2(t))/d$ and $w_a(t)=(w_1(t)+w_2(t))/d$ denote the bias and noise of the accelerometers, and $d=d_1+d_2$ denotes the distance between the two accelerometers. For most accelerometers, $b(t)$ can be accurately modeled as an exponentially correlated

Gaussian random process with a white noise $w_b(t)$ and correlation time τ as follows:

$$\dot{b}(t) = -b(t)/\tau + w_b(t) \tag{7}$$

The same chirp signal is used to investigate the angular velocity estimation of accelerometer unit. The inferred acceleration in Eq. (6) (scaled to unit of $(°)/s^2$) compared to the actual acceleration (second derivative of the high-resolution encoder) is shown in Figs. 5(a)-5(b) which show that an unknown bias is contained in the outputs of the accelerometer unit.

An intuitive approach to obtain velocity is to integrate the inferred acceleration of the accelerometer unit in Eq. (6). This approach is shown in Figs. 5(c)-5(d). It is clear that the estimated velocity obtained using accelerometer unit is only accurate in magnitude and phase over a wide range of frequencies. It has a fatal drawback in that the estimated error in magnitude will diverge over time due to the unknown bias term.

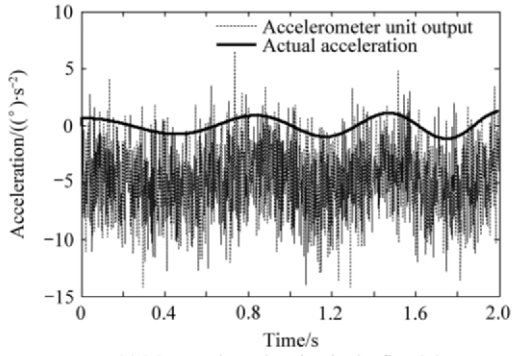

(a) Measured acceleration in the first 2.0 s

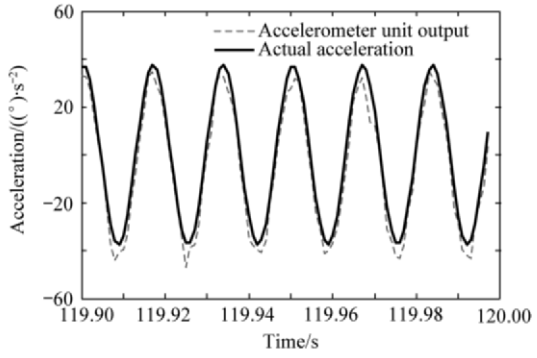

(b) Measured acceleration in the last 0.1 s

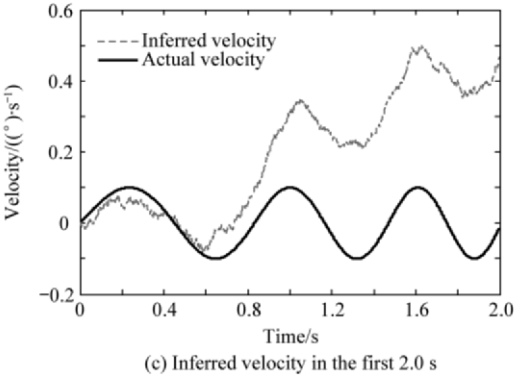

(c) Inferred velocity in the first 2.0 s

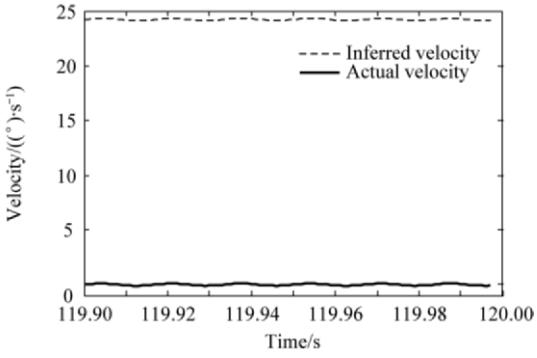

(d) Inferred velocity in the last 0.1 s

Fig. 5 Measured acceleration and inferred velocity of MEMS accelerometer unit in chirp motion.

3. Improved Angular Velocity Estimation

3.1. Structure of optimal velocity estimator

This section discusses the construction of an optimal state estimator meant to obtain high-performance velocity estimation by combining the inaccurate measurements from the gyroscope and the accelerometer unit. The hybrid system is shown in Fig. 6, where $\hat{\boldsymbol{x}}(t)$ denotes the estimation of the state vector.

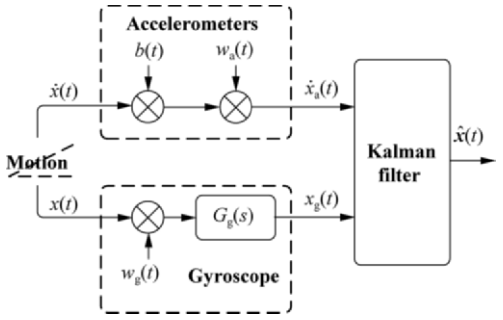

Fig. 6 Block diagram of the hybrid system.

From Eq. (3) and Eq. (6), the well-known state-space model is given as follows:

$$\begin{cases} \begin{bmatrix} \dot{x}(t) \\ \dot{b}(t) \\ \dot{x}_g(t) \\ \ddot{x}_g(t) \end{bmatrix} = \begin{bmatrix} 0 & -1 & 0 & 0 \\ 0 & -1/\tau & 0 & 0 \\ 0 & 0 & 0 & 1 \\ \omega_n^2 & 0 & -\omega_n^2 & -2\zeta\omega_n \end{bmatrix} \begin{bmatrix} x(t) \\ b(t) \\ x_g(t) \\ \dot{x}_g(t) \end{bmatrix} + \\ \qquad \begin{bmatrix} 1 \\ 0 \\ 0 \\ 0 \end{bmatrix} \dot{x}_a(t) + \begin{bmatrix} -1 & 0 & 0 \\ 0 & 1 & 0 \\ 0 & 0 & 0 \\ 0 & 0 & \omega_n^2 \end{bmatrix} \begin{bmatrix} w_a(t) \\ w_b(t) \\ w_g(t) \end{bmatrix} \\ x_g(t) = \begin{bmatrix} 0 & 0 & 1 & 0 \end{bmatrix} \begin{bmatrix} x(t) \\ b(t) \\ x_g(t) \\ \dot{x}_g(t) \end{bmatrix} + v(t) \end{cases} \tag{8}$$

This system can be rewritten in the standard continuous form as follows:

$$\begin{cases} \dot{\boldsymbol{x}}(t) = \boldsymbol{A}\boldsymbol{x}(t) + \boldsymbol{b}u(t) + \boldsymbol{G}\boldsymbol{w}(t) \\ y(t) = \boldsymbol{C}\boldsymbol{x}(t) + v(t) \end{cases} \tag{9}$$

where $\boldsymbol{x}(t) = [x(t) \quad b(t) \quad x_g(t) \quad \dot{x}_g(t)]^T$ is the state vector; $x(t)$, $b(t)$, $x_g(t)$ and $\dot{x}_g(t)$ are taken to be the actual velocity, the bias term of the accelerometer unit, the measurement and derivative measurement of the gyroscope, respectively; $u(t)=\dot{x}_a(t)$ and $y(t)=x_g(t)$ are the control and observed variables, respectively; $\boldsymbol{A}$, $\boldsymbol{b}$, $\boldsymbol{G}$ and $\boldsymbol{C}$ are defined in the obvious way; $\boldsymbol{w}(t)$ is the process noise and defined as follows:

$$E(\boldsymbol{w}(t)\boldsymbol{w}^T(\upsilon)) = \boldsymbol{Q}\delta(t-\upsilon) \tag{10}$$

where $\boldsymbol{Q} = \mathrm{diag}(\sigma_a^2, \sigma_b^2, \sigma_g^2)$ is the covariance matrix of the process noise, and δ the Kronecker operator. Because the covariance of the measurement noise $v(t)$ is a scalar, we represent it by r.

For the linear time-invariant system Eq. (9), an optimal state observer for velocity estimation is given by

$$\dot{\hat{\boldsymbol{x}}}(t) = \boldsymbol{A}\hat{\boldsymbol{x}}(t) + \boldsymbol{b}u(t) + \boldsymbol{K}(t)(y(t) - \boldsymbol{C}\hat{\boldsymbol{x}}(t)) \tag{11}$$

where $\boldsymbol{K}(t)=\boldsymbol{P}(t)\boldsymbol{C}^T r^{-1}$ denotes the observer gain, which is obtained by Kalman filter and calculated by a continuous Riccati equation as follows:

$$\dot{\boldsymbol{P}}(t) = \boldsymbol{A}\boldsymbol{P}(t) + \boldsymbol{P}(t)\boldsymbol{A}^T + \boldsymbol{G}\boldsymbol{Q}\boldsymbol{G}^T - \boldsymbol{P}(t)\boldsymbol{C}^T r^{-1}\boldsymbol{C}\boldsymbol{P}(t) \tag{12}$$

where $\boldsymbol{P}(t)$ is the covariance matrix of the estimation of the state vector, and $\boldsymbol{G}$ the transition matrix of the process noise.

In order to solve Eq. (12), let us first consider the following theorems.

Theorem 1 A linear time-invariant system is uniformly completely observable if and only if the observability matrix $\boldsymbol{M}$ shown in Eq. (13) has rank n (full column rank).

$$\boldsymbol{M} = [\boldsymbol{C} \quad \boldsymbol{C}\boldsymbol{A} \quad \cdots \quad \boldsymbol{C}\boldsymbol{A}^{n-1}]^T \tag{13}$$

Proof: See Ref. [16].

Theorem 2 Given any fixed initial time t_0 and a nonnegative definite matrix $\boldsymbol{P}_0$, Eq. (12) has a unique solution as follows:

$$\boldsymbol{P}(t) = \boldsymbol{\Pi}(t; \boldsymbol{P}_0, t_0) \tag{14}$$

where $\boldsymbol{P}_0$ is the initial value of $\boldsymbol{P}(t)$, which takes on the value $\boldsymbol{P}(t_0)=\boldsymbol{P}_0$ at $t=t_0$.

Proof: See Ref. [17].

Theorem 3 Assume the system is uniformly completely observable and the covariance matrix $\boldsymbol{Q}$ and r are constants. Every solution of Eq. (12) starting at a symmetric nonnegative matrix $\boldsymbol{P}_0$ converges to $\boldsymbol{P}(t)$ as $t\to\infty$. That is

$$\lim_{t\to\infty} \dot{\boldsymbol{P}}(t) = \boldsymbol{0} \tag{15}$$

Proof: See Ref. [18].

First, let us evaluate the rank of the observability matrix in Eq. (9).

$$\mathrm{rank}(\boldsymbol{M}) = \mathrm{rank}([\boldsymbol{C} \quad \boldsymbol{C}\boldsymbol{A} \quad \boldsymbol{C}\boldsymbol{A}^2 \quad \boldsymbol{C}\boldsymbol{A}^3]^T) = \mathrm{rank}\begin{bmatrix} 0 & 0 & 1 & 0 \\ 0 & 0 & 0 & 1 \\ \omega_n^2 & 0 & -\omega_n^2 & -2\zeta\omega_n \\ -2\zeta\omega_n^3 & -\omega_n^2 & 2\zeta\omega_n^3 & 4\zeta^2\omega_n^2 - \omega_n^2 \end{bmatrix} = 4 \tag{16}$$

According to Theorem 1, the system Eq. (9) is uniformly completely observable. Furthermore, we can set the initial matrix $\boldsymbol{P}_0$ as a nonnegative definite matrix artificially, and the hypotheses of Theorem 2 and Theorem 3 are satisfied. Then by substituting Eq. (15) into Eq. (12), the solution of the estimation problem is obtained by setting the right-hand side of Eq. (12) equal to zero and solving the following set of algebraic equations:

$$\boldsymbol{A}\boldsymbol{P}(\infty) + \boldsymbol{P}(\infty)\boldsymbol{A}^T + \boldsymbol{G}\boldsymbol{Q}\boldsymbol{G}^T = \boldsymbol{P}(\infty)\boldsymbol{C}^T r^{-1}\boldsymbol{C}\boldsymbol{P}(\infty) \tag{17}$$

Through the experiments in Section 2, we have found that the values of $\boldsymbol{Q}$=diag(2.15, 8.2, 0.13), r=0.064, ω_n=377 rad/s, ζ=0.707, τ=1 000 s, d=6 cm and T=1 ms. Taking those values into Eq. (17) and considering the matrixes $\boldsymbol{A}$, $\boldsymbol{G}$ and $\boldsymbol{C}$ in Eq. (8), the observer gain $\boldsymbol{K}(\infty)$ can be calculated using MATLAB, resulting in

$$\boldsymbol{K}(\infty) = [0.141 \quad -0.264 \quad 0.457\,6 \quad 106.7]^T \tag{18}$$

3.2. Angular velocity estimation error analysis

The static and dynamic tests will be explored in this section to analyze level of error in this method of angular velocity estimation.

(1) Noise statistics assessment

The static test, shown in Fig. 7, facilitates an assessment of the noise statistical properties of different methods. In this experiment, the test apparatus has been held static with zero velocity and acceleration, both serving as reference signals for comparison. Fig. 7(a) presents the comparison for the velocity estimation noise obtained by both gyroscope and Kalman filter. The value of the true velocity is taken to be zero in the static test. As shown in Fig. 7(a), the standard deviation of velocity estimation noise corresponding to the Kalman filter is 0.1 (°)/s, and that corresponding to the gyroscope is 0.284 (°)/s. The improvement is almost threefold. Fig. 7(b) depicts the respective power spectral density (PSD) of both gyroscope and Kalman filter. The noise PSD is reduced by

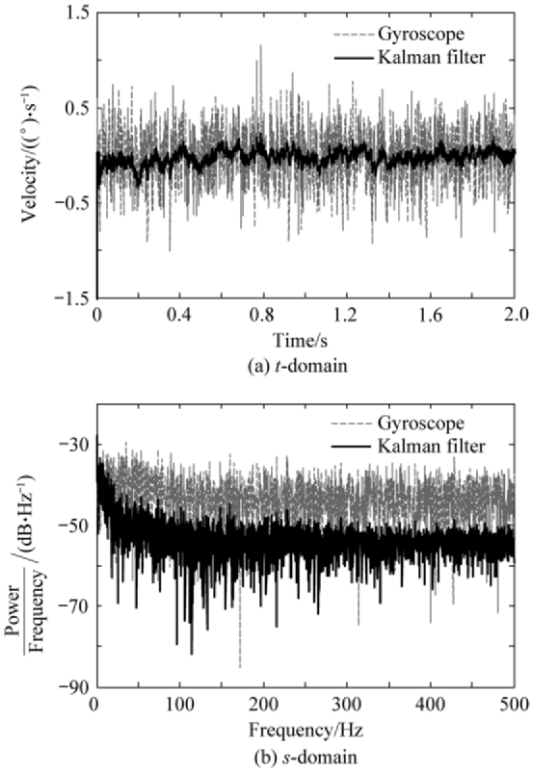

Fig. 7 Statistical noise assessment of different methods.

more than 10 dB in magnitude, corresponding to the gyroscope.

(2) Dynamic motion validation

The dynamic test, shown in Fig. 8, has been executed to verify and demonstrate the ability of the methods to track the dynamic motion profile. Consider the following arbitrary velocity signal [19] with a wide range of frequency components given as follows:

$$\omega_r = 0.2\sin(2\pi t) + 2e^{-20(t-2)^2}\sin(15\pi t + 1) \quad (19)$$

The exponential term of Eq. (19) is used as a weighting factor, which yields the high-frequency components around 2 s. Note that the high-resolution encoder is used because its first derivatives provide an accurate reference velocity ω_r. The gyroscope's velocity measurements, shown in Fig. 8(a), provide inaccurate results over a wide range of velocities, while those based on the accelerometer unit, shown in Fig. 8(b), diverge over time. However, the Kalman filter used to fuse the sensors, shown in Fig. 8(c), has a good velocity response over a wide range of velocities. Fig. 8(d)

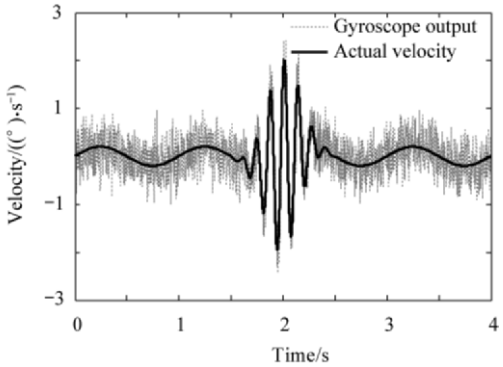

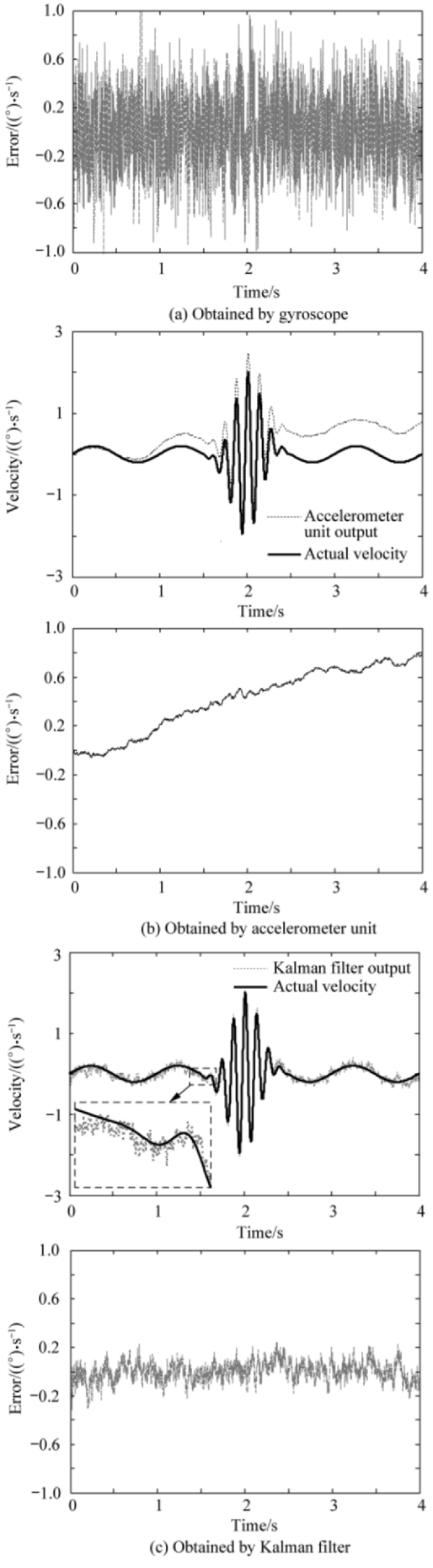

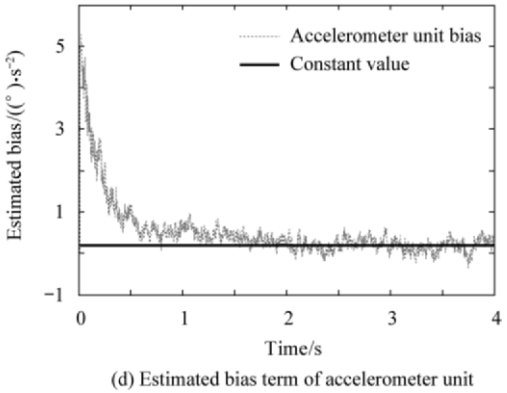

(d) Estimated bias term of accelerometer unit

Fig. 8 Angular velocity estimations obtained by different methods.

shows the estimation of the accelerometers' bias term to converge to a value of b=0.2 (°)/s^2 in about 1 s, which can be compensated online. It also shows that the observed bias term varies during motion.

4. Applications in Mini-ISP Control System

ISPs have seen wide use in scientific, military, and commercial applications [1-2]. In this section, the modeling and control problems of ISP will be briefly reviewed.

4.1. Modeling of mini-ISP control system

ISP is usually configured with a high-bandwidth stabilized-loop to hold inertial stationary of the optical sensors' LOS in spite of any inner or outer disturbance. Fig. 9 shows a block diagram of the control system for a one degree-of-freedom mini-ISP.

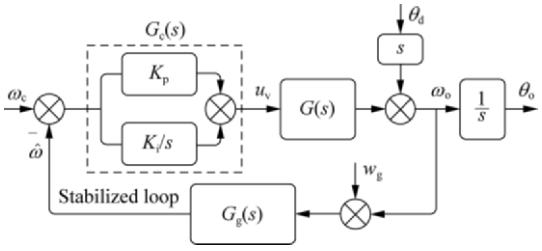

Fig. 9 Block diagram of control system for one degree-of-freedom mini-ISP.

In Fig. 9, $G(s)$ is the dynamics of the power amplifier, motor and platform, $G_c(s)$ the velocity controller, K_p and K_i denote proportional gain and integral gain of $G_c(s)$ respectively, ω_c and ω_o the velocity command and output of the control system, respectively, $\hat{\omega}$ and w_g the measured signal and noise of gyroscope respectively, θ_d and θ_o the attitude disturbance and angle output of the mini-ISP, u_v is the control signal sent to the power amplifier.

There are two fundamental issues with regard to choosing a control structure for an ISP. One is that the stabilized loop attempts to nullify the difference between the command and the output. The Laplace transform of velocity output can be written as

$$\omega_o = \frac{G_c(s)G(s)}{1+G_g(s)G_c(s)G(s)}\omega_c + \frac{s}{1+G_g(s)G_c(s)G(s)}\theta_d - \frac{G_g(s)G_c(s)G(s)}{1+G_g(s)G_c(s)G(s)}w_g \tag{20}$$

The other is that the stabilized loop attempts to reject the disturbance caused by various error sources, such as θ_d and w_g, etc. When the velocity command ω_c is zero or absent, the angle outputs of mini-ISP θ_o can be illustrated as

$$\theta_o = \frac{1}{s}\omega_o = \frac{\theta_d}{1+G_g(s)G_c(s)G(s)} - \frac{G_g(s)G_c(s)G(s)/s}{1+G_g(s)G_c(s)G(s)}w_g \tag{21}$$

To achieve optimal velocity tracking performance and disturbance rejection, the controller is found by solving the following constrained optimization problem in [20]

$$\min \| T_{\omega_o\to\omega_c}(s)\|_\infty \tag{22}$$

subject to

1) The amplitude gain of $P_l(s) > \sigma_1$ at frequency f_1.

2) The phase margin of $P_l(s) > \sigma_2$ at frequency f_2.

where $T_{\omega_o\to\omega_c}(s)$ is the transfer function from ω_o to ω_c, $P_l(s)=G_g(s)G_c(s)G(s)$ the open-loop transfer function of the stabilized loop, σ_1 and σ_2 are amplitude gain and phase margin bounds respectively, f_1 denotes the nature of the specific aircraft that the mini-ISP is mounted on, and f_2 denotes the bandwidth of the control system.

4.2. Improving of mini-ISP control performance

For practical reasons, a conventional proportional-integral (PI) controller [21-22], which is structurally simple and intuitive to tune, has been adopted to solve Eq. (22). The control signal u_v is given by

$$u_v = K_p(\omega_c - \hat{\omega}) + K_i\int(\omega_c - \hat{\omega})\mathrm{d}t \tag{23}$$

Table 2 shows the PI controller parameters and the constraint limits of gyroscope feedback.

Table 2 Controller parameters and constraint limits

σ_1/dB	f_1/Hz	σ_2/(°)	f_2/Hz	K_p	K_i
20	1	60	40	4.1	46.6

For the first issue, the step and sinusoidal velocity profile are executed to illustrate the improved performance using high-quality signal obtained by the proposed Kalman filter relative to gyroscope feedback. The conventional PI controller is with proportional gain K_p=4.1 and integral gain K_i=46.6. It can be observed that the overshoot has been reduced from 50.4% to 5.3%, shown in Fig. 10(a), and the mean square deviation of velocity tracking error with gyro-

scope feedback is 0.327 (°)/s. With Kalman filter feedback, it is 0.086 (°)/s, shown in Fig. 10(b).

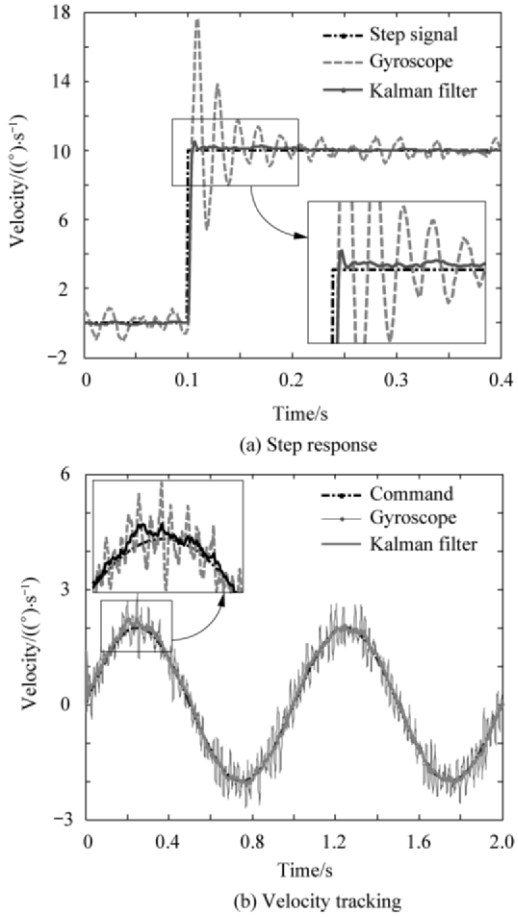

Fig. 10 Comparison of control performance for stabilized loop with gyroscope feedback and Kalman filter feedback.

For the second consideration, the disturbance rejection performance is evaluated. The PI controllers are with K_p=4.1 and K_i=46.6 for gyroscope feedback, and with K_p=19.1 and K_i=211.3 for Kalman filter feedback. The magnitude of transfer function from θ_d to θ_o, denoted as $T_{\theta_d\to\theta_o}(s)$, is plotted in Fig. 11(a). And the attitude disturbance θ_d coupled with the aircraft's natural modes and the platform's base vibration is depicted in Fig. 11(b). This occurs predominantly at the frequency and amplitude of 1 Hz and 1° peak-to-peak respectively. It should be noted that the magnitude of $|T_{\theta_d\to\theta_o}(s)|$ with gyroscope feedback is −18.5 dB, while with Kalman filter feedback it is −32.6 dB at this typical frequency. Disturbance rejection performance has been improved by almost 14 dB.

Figs. 11(c)-11(d) show the velocity output ω_o and the angle output θ_o with different feedbacks, when the velocity command ω_c is zero and the platform base is excited by this attitude disturbance θ_d only. The angle of the platform's LOS is limited within −0.15°-0.15° for the gyroscope, and 0°-0.1° for Kal- man filter. It can also be seen that the angle will diverge over time due to the drift of the gyroscope.

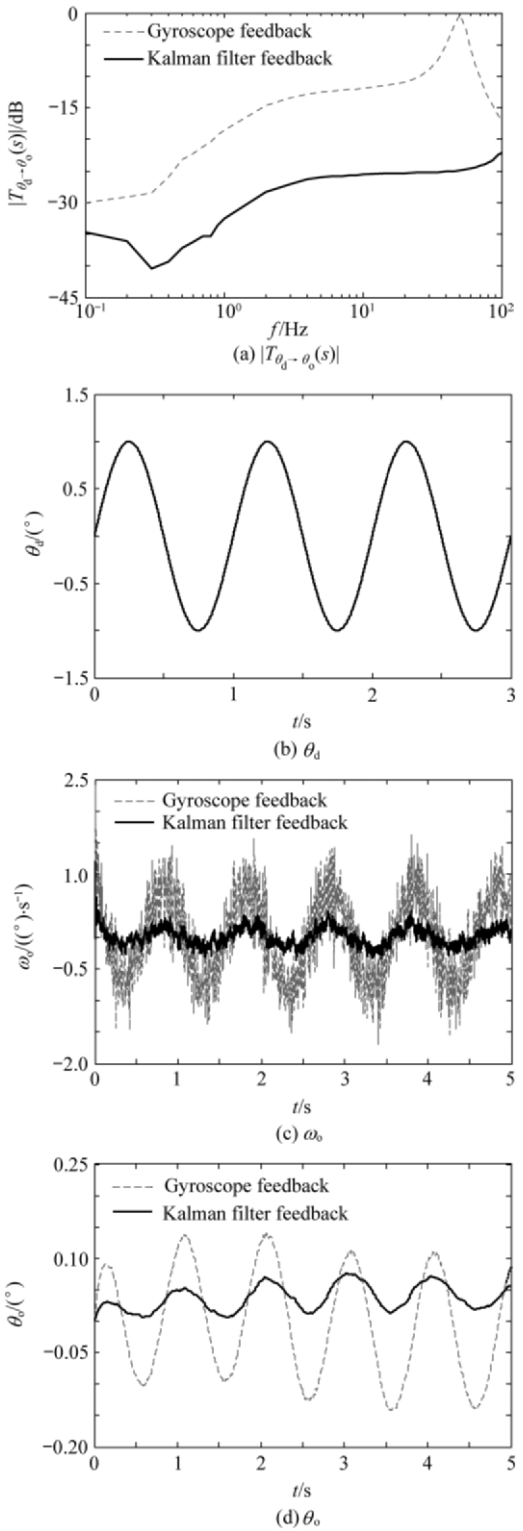

Fig. 11 Disturbance rejection performance of stabilized loop with gyroscope feedback and Kalman filter feedback.

5. Conclusions

This paper analytically and experimentally shows

that MEMS gyroscope yields inaccurate and low-bandwidth measurements of angular velocity. To overcome this problem, an improved velocity estimation algorithm has been developed using a combination of a MEMS gyroscope and accelerometers. Static and dynamic experiments show that the proposed method can yield accurate signals over a wide range of velocities in both the *t*- and *s*-domains.

The proposed angular velocity estimator can also be applied to the control system of a miniature inertially stabilized platform in order to verify its validity. With this estimator, the overshoot of step response and the error of sinusoidal velocity tracking have been significantly reduced. Furthermore, disturbance rejection performance can also be significantly improved. This is attributed to the accurate and high-bandwidth signals provided by the proposed estimator.

References

[1] Hilkert J M. Inertially stabilized platform technology. IEEE Control Systems 2008; 28(1): 26-46.

[2] Masten M K. Inertially stabilized platforms for optical imaging systems. IEEE Control Systems 2008; 28(1): 47-64.

[3] Gawronski W. Control and pointing challenges of large antennas and telescopes. IEEE Transactions on Control Systems Technology 2007; 15(2): 276-288.

[4] Ghommam J, Mehrjerdi H, Saad M. Coordinated path-following control for a group of mobile robots with velocity recovery. Proceedings of the Institution of Mechanical Engineers, Part I: Journal of Systems and Control Engineering 2010; 225 (5): 995-1006.

[5] Luinge H J, Veltink P H, Baten C T M, et al. Estimation of orientation with gyroscope and accelerometers. Proceedings of the First Joint BMES/EMBS Conference. 1999; 2: 844.

[6] Fang J C, Zhang X, Li J L. A compensation method for MEMS gyro scale factor error. Acta Aeronautica et Astronautica Sinica 2010; 31(2): 350-355. [in Chinese]

[7] Xiao W G, Ding M L, Wang Q. Application of total least square algorithm in static decoupling of NGMIMU. Acta Aeronautica et Astronautica Sinica 2004; 17(4): 224-228. [in Chinese]

[8] Cui M, Ma T H, Zhang M. Research on calibration and error compensation for GFSINS. Journal of Electronic Measurement and Instrument 2009; 23(9): 23-26. [in Chinese]

[9] Cheng Y, Yang D, Cui H T. Gyroless attitude and rate estimation using singer model. Acta Aeronautica et Astronautica Sinica 2002; 23(6): 507-511. [in Chinese]

[10] Algrain M C. Accelerometer-based platform stabilization. SPIE Acquisition, Tracking, and Pointing. 1991; 367-382.

[11] Zhu W H, Lamarche T. Velocity estimation by using position and acceleration sensors. IEEE Transactions on Industrial Electronics 2007; 54(10): 2706-2714.

[12] Jeon S, Tomizuka M. Benefits of acceleration measurement in velocity estimation and motion control. Control Engineering Practice 2005; 15(12): 325-332.

[13] Leavitt J, Sideris A. High bandwidth tilt measurement using low-cost sensors. IEEE/ASME Transactions on Mechatronics 2006; 11(3): 320-327.

[14] Rehbinder H, He X M. Nonlinear pitch and roll estimation for walking robots. Proceedings of IEEE International Conference on Robotics and Automation. 2000; 2617-2622.

[15] Ojeda L, Borenstein J. FLEXnav: fuzzy logic expert rule-based position estimation for mobile robots on rugged terrain. Proceedings of IEEE International Conference on Robotics and Automation. 2002; 317-322.

[16] Skogestad S, Postlethwaite I. Multivariable feedback control analysis and design. Hoboken, NJ: John Wiley & Sons, Inc., 1996: 135-137.

[17] Kalman R E. Contributions to the theory of optimal control. Proceedings of Ordinary Differential Equations Conference. 1959; 147-166.

[18] Kalman R E, Bucy R S. New results in linear filtering and prediction theory. Transactions of the ASME 1961; 83: 95-107.

[19] Lee S H, Song J B. Acceleration estimation for low-velocity and low-acceleration regions based on encoder position data. IEEE/ASME Transactions on Mechatronics 2001; 6(1): 58-64.

[20] Yeh T J, Su C Y, Wang W J. Modeling and control of a hydraulically actuated two-degree-of-freedom inertial platform. Proceedings of the Institution of Mechanical Engineers, Part I: Journal of Systems and Control Engineering 2005; 219(6): 405-417.

[21] Yaron Z, Yaakkov O, Amit B. Improving the accuracy of analog encoders via Kalman filtering. Control Engineering Practice 2006; 14(4): 337-350.

[22] Raman J, Cretu E, Rombouts P, et al. A closed-loop digitally controlled MEMS gyroscope with unconstrained sigma-delta force-feedback. IEEE Sensors Journal 2009; 9(3): 297-305.

Biographies:

ZHOU Xiaoyao Born in 1982, he received B.S and M.S. degrees in mechanical engineering from the Second Artillery Engineering Institute, Xi'an, China, in 2004 and 2007 respectively. Currently he is a Ph.D. candidate at College of Mechatronics and Automation, National University of Defense Technology, Changsha, China. His current research interests include nonlinear control and error analysis of optical pointing systems.
E-mail: zhouxiaoyao2004@yahoo.com.cn

ZHANG Zhiyong Born in 1979, he received Ph.D. degree in mechanical engineering from National University of Defense Technology, Changsha, China. Currently he is with National University of Defense Technology as a teacher of College of Mechatronics and Automation. He has designed more than 20 precision optical systems for surveillance, target tracking, missile guidance, fire control, and laser communication. His scientific interests include optical imaging system, ultra-precision measurement, error analysis, and motion control.
E-mail: zzynihao@126.com